

Probing hidden spin-2 mediator of dark matter with NA64 $_e$, LDMX, NA64 $_\mu$ and M 3

I. V. Voronchikhin^{1,*} and D. V. Kirpichnikov^{2,†}

¹*Tomsk Polytechnic University, 634050 Tomsk, Russia*

²*Institute for Nuclear Research, 117312 Moscow, Russia*

(Dated: October 4, 2022)

The connection between Standard Model (SM) particles and dark matter (DM) can be introduced via hidden spin-2 massive mediator. In the present paper we consider the simplified benchmark link between charged lepton sector of SM and DM particles which are considered to be a hidden Dirac fermions from the dark sector. The regarding couplings are established through the dimension-5 operators involving spin-2 mediator field and the energy-momentum tensors of both SM and DM sectors. We study in detail the implication of this scenario for the lepton fixed-target facilities, such as NA64 $_e$, LDMX, NA64 $_\mu$ and M 3 . In particular, for the specific experiment we discuss in detail the missing-energy signatures of spin-2 boson production followed by its invisible decay into stable DM pairs. Moreover, we derive the expected reaches of these experiments for the projected statistics of the leptons accumulated on the target. We also discuss the implication of both nuclear and atomic form-factor parametrizations for the differential spectra of hidden spin-2 boson emission, the total cross-section of its production and the experimental reach of the fixed-fixed target facilities for probing hidden spin-2 DM mediator.

I. INTRODUCTION AND FRAMEWORK

The nature of the dark matter (DM) particles remains puzzling for decades. The indirect evidences for the DM are associated with galaxy rotation velocities, large scale structures, cosmic microwave background anisotropy, gravitational lensing, etc. Some extensions of the standard model (SM) imply connection between SM and DM via an idea of portals. For instance, the dark photon portal [1–4] and Higgs boson portal [5–8]. Such portal scenarios suggest a systematic probing of DM and also provide a novel specific experimental signatures. However, recently a scenarios of a massive spin-2 particle as the mediator between DM and SM have been discussed [9–13] in the context of gravity model with warped extra-dimensions [14–21]. Furthermore, recently confirmed 4.2σ discrepancy in the anomalous magnetic moment measurement of the muon [22] with respect to its theoretical prediction [23]:

$$\Delta a_\mu = a_\mu(\text{exp}) - a_\mu(\text{th}) = (251 \pm 59) \times 10^{-11},$$

can be explained by the one-loop effects induced by a hidden massive spin-2 particle [10, 24]. Let us consider now the couplings between the charged lepton sector of the SM and the DM particles that can be described by the benchmark simplified Lagrangian [10] involving dimension-5 operators of the energy momentum tensor and massive $G_{\mu\nu}$ field:

$$\begin{aligned} \mathcal{L} \supset & \frac{c_\gamma}{\Lambda} G^{\mu\nu} \left(\frac{1}{4} \eta_{\mu\nu} F_{\lambda\rho} F^{\lambda\rho} + F_{\mu\lambda} F_\nu^\lambda \right) \\ & - \sum_l \frac{ic_l}{2\Lambda} G^{\mu\nu} (\bar{l} \gamma_\mu D_\nu l - \eta_{\mu\nu} \bar{l} \gamma_\rho D^\rho l) + \frac{c_\chi}{\Lambda} G^{\mu\nu} T_{\mu\nu}^\chi, \quad (1) \end{aligned}$$

where $F_{\mu\nu}$ is stress tensor for the photon field, l is the label for the charged leptons ($l = e, \mu$), Λ is dimensional parameter for spin-2 interactions, c_γ , c_l , c_χ are the dimensionless coupling constants for the electromagnetic field, charged leptons of SM and DM sector respectively; $T_{\mu\nu}^\chi$ is the energy momentum tensor of DM particles. To be more concrete we address DM as hidden Dirac fermion χ with mass of m_χ . In addition, it is worth noting that the coupling constants in the regarding scenario are assumed to be independent.

In the present paper we show that corresponding setup (1) has a very broad phenomenological implication and can be examined through the missing energy signatures in the existent (NA64 $_e$ [25–37] and NA64 $_\mu$ [38, 39]) and the projected (LDMX [40–43] and M 3 [44, 45]) lepton fixed-target experiments. These signatures can be described by the bremsstrahlung-like reaction of the production of a spin-2 boson by the charged lepton l^- impinging on a nucleus N . The corresponding diagrams are shown in Fig. 1. In the present paper we will focus on mainly invisible channel of dark spin-2 boson decay into DM particles, such that $\text{Br}(G \rightarrow \chi\bar{\chi}) \simeq 1$. Furthermore, for the G -boson production cross-section calculation we exploit the equivalent photons approximation, also known as the Weizsacker–Williams (WW) approach that is typically exploited for the hidden particle yield estimate at both beam dump and fixed-target experiments. In particular, this approach provides a fairly reasonable approximation (i. e. at the level of $\lesssim 2\%$) for the exact-tree-level production cross-sections of both hidden spin-0 and spin-1 bosons [39, 46, 47].

In addition, we also discuss in detail the impact of both nuclear and atomic form-factor parametrizations on: (i) the differential spectra of G boson emission, (ii) the total cross-section of its production (iii) the experimental reach of the fixed-fixed target facilities for probing hidden spin-2 boson.

The paper is organized as follows. In Sec. II we derive

* Corresponding author; e-mail: ivv1211@yandex.ru

† e-mail: dmbrick@gmail.com

explicitly the double differential cross-section of G -boson production in WW approach. In Sec. III we discuss the set of form-factors that are typically used for the calculation of regarding cross-sections. In this section we also study the impact of various form-factor parametrizations on the virtual photon flux distribution from the charged particles. In Sec. IV we provide a description of the missing energy signatures for the analysis of DM production at lepton fixed-target experiments, such as NA64e, LDMX, NA64 μ and M³. In Sec. V we discuss the impact of form-factor parametrization on both differential and total cross-sections of hidden spin-2 boson production. In Sec. VI we obtain the constraints on the parameter space of spin-2 DM mediator from the NA64e, LDMX, NA64 μ and M³ facilities. In this section we also study implication of the form-factors for the expected reach of the regarding experiments.

II. THE PRODUCTION CROSS SECTION OF DM MEDIATOR IN WW APPROACH

Let us consider the kinematic variables of bremsstrahlung-like process $2 \rightarrow 3$ in the laboratory frame:

$$l^-(p) + N(P_i) \rightarrow l^-(p') + N(P_f) + G(k), \quad (2)$$

where $p = (E_l, \mathbf{p})$ is the momentum of incoming charged lepton, $p' = (E_l', \mathbf{p}')$ is the momentum of outgoing lepton, $k = (E_G, \mathbf{k})$ is the momentum of spin-2 mediator, $P_i = (M, 0)$ and $P_f = (P_f^0, \mathbf{P}_f)$ are the momenta of the initial and outgoing nucleus respectively. We define four-momentum transfer to nucleus as $P_i - P_f = q = (q_0, \mathbf{q})$, such that the photon virtuality takes the form $t = -q^2 > 0$. In order to calculate the differential cross-section of G boson production in nuclear interaction one can exploit the Weizsäcker-Williams approximation, implying that the energy of incoming lepton is much higher than m_l and m_G . In this case, the incoming charged particle is replaced by its effective photon flux, such that the phase space of the process $l^-(p)N(P_i) \rightarrow l^-(p')N(P_f)G(k)$ is reduced to the Compton-like process $l^-(p)\gamma(q) \rightarrow l^-(p')G(k)$. In particular, one can obtain the following expression for the double differential cross-section [48–50]:

$$\begin{aligned} & \frac{d\sigma(p + P_i \rightarrow p' + P_f + k)}{d(pk)d(kP_i)} \Big|_{WW} = \\ & = \frac{\alpha\chi}{\pi(p'P_i)} \frac{d\sigma(p + q \rightarrow k + p')}{d(pk)} \Big|_{t=t_{min}}, \end{aligned} \quad (3)$$

where the flux of virtual photon χ from nucleus is expressed through the elastic form-factor $F(t)$ as follows:

$$\chi = Z^2 \int_{t_{min}}^{t_{max}} \frac{t - t_{min}}{t^2} F^2(t) dt, \quad (4)$$

where Z is the atomic number of the nucleus, the explicit expressions for the form-factors $F(t)$ are discussed below in Section III. The photon flux for the inelastic form-factor is proportional to $\propto Z$, and thus can be ignored in the calculation for heavy nuclei $Z \propto \mathcal{O}(100)$. The WW approach in Eqs. (3) and (4) implies that the virtuality t has its minimum $t = t_{min}$ when \mathbf{q} is collinear with $\mathbf{k} - \mathbf{p}$. In particular, the expression for t_{min} is derived below (see, e. g. Eq. (11)). For ultra-relativistic incident lepton in laboratory frame we have:

$$\begin{aligned} d(kp)d(kP_i) & \simeq |\mathbf{J}(\cos(\theta_G), E_G)| d\cos(\theta_G) dE_G \simeq \\ & \simeq M |\mathbf{p}| |\mathbf{k}| d\cos(\theta_G) dE_G, \end{aligned} \quad (5)$$

where θ_G is the angle between the initial lepton direction and the momentum of the produced G -boson and $\mathbf{J}(\cos(\theta_G), E_G)$ is the Jacobian of the transformation from (kp) and (kP_i) variables to $\cos \theta_G$ and E_G . So that by substituting Eq. (5) into Eq. (3), we get the following expression for the double differential cross-section after some algebraic simplification:

$$\begin{aligned} & \frac{d\sigma(p + P_i \rightarrow p' + P_f + k)}{dx d\cos(\theta_G)} \Big|_{WW} = \\ & \frac{\alpha\chi}{\pi} \frac{E_l^2 x \beta_G}{1-x} \frac{d\sigma(p + q \rightarrow k + p')}{d(pk)} \Big|_{t=t_{min}}, \end{aligned} \quad (6)$$

where $\alpha = e^2/(4\pi) \simeq 1/137$ is the fine structure constant, $x = E_G/E_l$ is the energy fraction of spin-2 mediator that it carries away and $\beta_G = \sqrt{1 - m_G^2/(xE_l)^2}$ is the typical velocity of G -boson. By solving the mass-shell equations for both outgoing electron and nucleus:

$$p'^2 = (q + p - k)^2 = m_l^2, \quad P_f^2 = (P_i - q)^2 = M^2, \quad (7)$$

we get the following auxiliary expressions: $q_0 = -t/(2M)$ and $|\mathbf{q}|^2 = t^2/(4M^2) + t$. Furthermore, by taking into account the small typical energy transferred to the nucleus $|\mathbf{q}|/M \ll 1$, we get both approximate expressions $t \simeq |\mathbf{q}|^2$ and $q_0 \simeq -|\mathbf{q}|^2/(2M)$ for the photon virtuality and nucleus energy transfer respectively. The value of q_0 is fairly small and thus can be neglected in the calculation, since the typical momentum is $|\mathbf{q}| \lesssim \mathcal{O}(100)$ MeV and the mass of nucleus is of the order of $M \propto \mathcal{O}(100)$ GeV. On the other hand, the photon flux χ is sensitive to the photon virtuality $t \simeq |\mathbf{q}|^2$, as long as the screening effects due to the atomic electrons should be taken into account (see e. g. Sec. III for detail).

Next, let us introduce the Mandelstam variables in the following form:

$$s_2 = (p + q)^2, \quad u_2 = (p - k)^2, \quad t_2 = (p - p')^2. \quad (8)$$

It is worth mentioning that Eq. (7) implies, $q_0^2 - |\mathbf{q}|^2 + u_2 + 2q_0V_0 - 2(\mathbf{q}, \mathbf{V}) = m_l^2$, where we define the three-vector as $\mathbf{V} = \mathbf{p} - \mathbf{k}$. Then for the small energy transferred to the nucleus $|\mathbf{q}|^2 \ll s_2, t_2, u_2$, one obtains:

$$t = \frac{(u_2 - m_l^2)^2}{4|\mathbf{V}|^2 \cos^2(\theta_{\mathbf{q}\mathbf{V}})}, \quad (9)$$

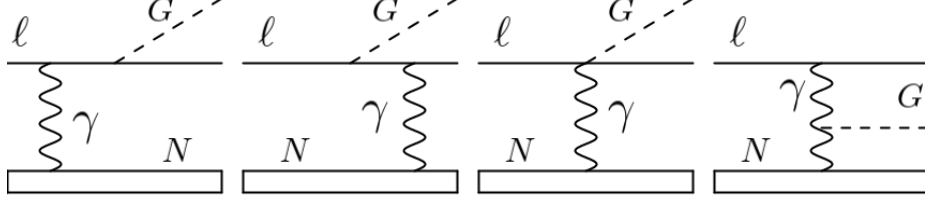


Figure 1. Feynman diagrams describing missing energy signatures.

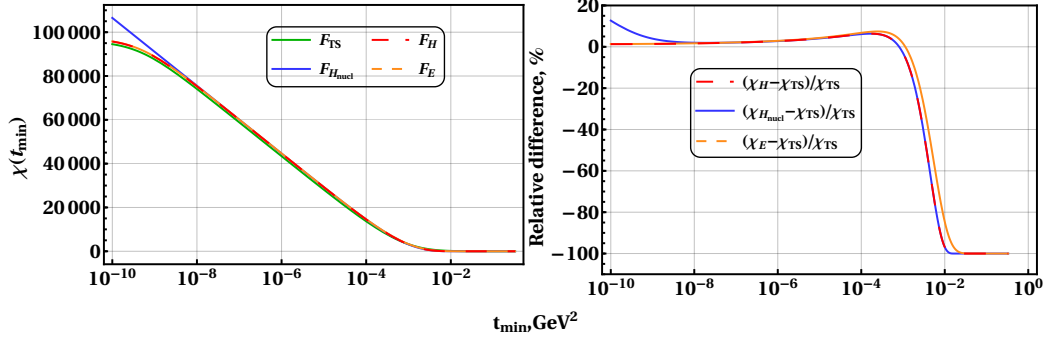


Figure 2. Left panel: virtual photon flux for Tsai-Schiff's F_{TS} (the green solid line), nuclear Helm's $F_{H_{nucl}}$ (the blue solid line), atomic Helm's F_H (the red dashed line) and atomic exponential F_E (the orange dashed line) form-factors as function of the lower limits t_{min} with fixed upper limit $t_{max} = 10 \text{ GeV}^2$. Right panel: the relative difference between benchmark Tsai-Schiff's flux and other fluxes.

where $\theta_{\mathbf{qV}}$ is the angle between vector \mathbf{q} and \mathbf{V} . Therefore keeping only leading terms in m_G^2/E_k^2 , m_l^2/E_l^2 , $m_{l'}^2/E_{l'}^2$ and θ_G^2 , we obtain the approximate expression for the absolute value of the three vector, $|\mathbf{V}| \simeq E_l(1-x)$. Let us introduce the following auxiliary function:

$$U \equiv m_l^2 - u_2 \simeq E_l^2 \theta_G^2 x + m_G^2(1-x)/x + m_l^2 x > 0, \quad (10)$$

thus by exploiting Eqs. (9) and (10) one can obtain the expressions for minimum of the virtuality $t = t_{min}$, implying that $\theta_{\mathbf{qV}} \simeq \pi$, such that the three vector \mathbf{q} is almost collinear with $\mathbf{k} - \mathbf{p}$:

$$t_{min} \simeq |\mathbf{q}|^2 \simeq U^2 / (4E_l^2(1-x)^2). \quad (11)$$

It is worth noting that the WW approximation for the $2 \rightarrow 3$ cross-section implies that t_{min} is the function of both x and θ_G variables, so that it is fairly accurate approach for the exact tree level cross-section (for de-

tail, see, e. g. Ref. [39] and references therein). Moreover, we note that $\theta_{\mathbf{qp}} \simeq \pi$ as long as $\theta_G \ll 1$ and \mathbf{q} is collinear with $\mathbf{k} - \mathbf{p}$, therefore this yields, $(q, k) \simeq |\mathbf{q}||\mathbf{k}| \simeq Ux/(2(1-x))$, and we finally get the following expressions for Mandelstam terms expressed through the both x and θ_G variables:

$$u_2 = m_l^2 - U \lesssim 0, \quad (12)$$

$$t_2 = -2(q, k) + t + m_G^2 \simeq -Ux/(1-x) + m_G^2 \lesssim 0, \quad (13)$$

$$s_2 = 2m_l^2 + m_G^2 - t - t_2 - u_2 \simeq U/(1-x) + m_l^2 \gtrsim 0. \quad (14)$$

Note that both the energy conservation law, $q_0 + E_l = E_l' + E_G$, and the condition, $q_0/E_l \ll 1$, imply that $E_l \simeq E_G + E_l'$, thus for the energy fraction $x = E_G/E_l$ we get respectively its minimum and maximum values in the following form $\hat{x}_{min} \simeq m_G/E_l$ and $\hat{x}_{max} \simeq 1 - m_l/E_l$.

By exploiting FeynCalc package [51, 52] for the Wolfram Mathematica routine [53], we get matrix element for process $l^- \gamma \rightarrow l^- G$ (see e. g. Appendix (A)):

$$|\mathcal{M}_{l^- \gamma \rightarrow Gl^-}|^2 = \frac{c_l^2 e^2}{\Lambda^2} \frac{u_2 [s_2 - 2m_l^2] [(t_2 + u_2)^2 + (u_2 - m_G^2)^2] [4u_2(2m_l^2 - s_2) - m_G^2 t_2]}{4t_2(u_2 - m_l^2)^2 (s_2 - m_l^2)^2} - \frac{c_l^2 e^2}{\Lambda^2} \frac{m_l^2 R(m_l, m_G, t_2, u_2)}{12t_2^2(m_l^2 - u_2)^2 (s_2 - m_l^2)^2}, \quad (15)$$

where $R(m_l, m_G, t_2, u_2)$ is regular expression for m_l and m_G that is given in the Appendix A. Note that in Eq. (15) we set universal coupling of G boson to both charged lepton and photon, such that $c_l \equiv c_e = c_\mu = c_\gamma$. It implies that the unitarity of the scenario is not violated at low energies as soon as $m_G \rightarrow 0$ (see, e. g. Ref. [10] and references therein for detail). The differential cross section for process $2 \rightarrow 2$ is

$$\frac{d\sigma_{2 \rightarrow 2}}{d(pk)} = 2 \frac{d\sigma_{2 \rightarrow 2}}{du_2} = \frac{1}{8\pi(s_2 - m_l^2)^2} |\mathcal{M}_{l-\gamma \rightarrow Gl-}|^2, \quad (16)$$

where $|\mathcal{M}_{l-\gamma \rightarrow Gl-}|^2$ is defined by (15). As a result, the double-differential cross section of the bremsstrahlung-like process $lN \rightarrow lNG(\rightarrow \chi\bar{\chi})$ takes the following form:

$$\begin{aligned} \left. \frac{d\sigma(p + P_i \rightarrow p' + P_f + k)}{dx d\cos(\theta_G)} \right|_{WW} &= \\ &= \frac{\alpha\chi}{\pi} \frac{E_l^2 x \beta_G}{1-x} \frac{1}{8\pi(s_2 - m_l^2)^2} |\mathcal{M}_{l-\gamma \rightarrow Gl-}|^2. \end{aligned} \quad (17)$$

In order to verify our calculation for the matrix element squared of spin-2 particle production $e^-(p)\gamma(q) \rightarrow G(k)e^-(p')$ one can exploit the crossing symmetry for the well known process of electron positron pair annihilation $e^+(p_{e+})e^-(p_{e-}) \rightarrow G(p_G)\gamma(p'_\gamma)$, for which the amplitude squared can be found in Ref. [10]. In particular, for the massless fermion the regarding transition element reads as follows [10]:

$$\begin{aligned} |\mathcal{M}_{e^+e^- \rightarrow \gamma G}|^2 &= \\ &= \frac{c_e^2 e^2}{\Lambda^2} \frac{(\hat{s}_2^2 + 2\hat{t}_2(\hat{s}_2 + \hat{t}_2) - 2m_G^2\hat{t}_2 + m_G^4)}{4\hat{t}_2\hat{s}_2(\hat{s}_2 + \hat{t}_2 - m_G^2)} \times \\ &\times (4\hat{t}_2(\hat{s}_2 + \hat{t}_2) - m_G^2(\hat{s}_2 + 4\hat{t}_2)), \end{aligned} \quad (18)$$

where the Mandelstam variables are defined by:

$$\hat{s}_2 \equiv (p_{e-} + p_{e+})^2, \quad \hat{t}_2 \equiv (p_{e-} - p'_G)^2, \quad \hat{u}_2 \equiv (p_{e-} - p'_\gamma)^2. \quad (19)$$

The crossing-symmetry implies the momentum replacement for the initial process $e^+e^- \rightarrow \gamma G$ in the following form: $p_{e+} \rightarrow -p'_{e-}$ and $p'_\gamma \rightarrow -p_\gamma$. The regarding Mandelstam variables transform as follows: $\hat{s}_2 \rightarrow t_2$, $\hat{t}_2 \rightarrow u_2$ and $\hat{u}_2 \rightarrow s_2$, where the notations for s_2, u_2 and t_2 are introduced (see e. g. Eq. (8)) in order to match with conventional labels of the authors of Ref. [50]. Finally this yields the following expression for the matrix element squared:

$$\begin{aligned} |\mathcal{M}_{e^-\gamma \rightarrow Ge^-}|^2 &= \\ &= \frac{c_e^2 e^2}{\Lambda^2} \frac{(t_2^2 + 2u_2(u_2 + t_2) - 2m_G^2u_2 + m_G^4)}{4u_2t_2(u_2 + t_2 - m_G^2)} \times \\ &\times (4u_2(u_2 + t_2) - m_G^2(t_2 + 4u_2)) \end{aligned} \quad (20)$$

It is worth noting that Eq. (15) tends to Eq. (20) in the massless lepton limit as soon as $m_l \rightarrow 0$.

III. THE VIRTUAL PHOTON FLUX FUNCTION

In this section we discuss the impact of different atomic and nuclear form-factor parametrization $F(t)$ for the photon flux χ which is given by Eq. (4). The latter affects the differential and total cross sections of hidden spin-2 boson production, that will be discussed in Section V.

The nuclear form-factor in the laboratory frame is associated with charge density of nucleus through the Fourier transformation for both spin-0 and spin-1/2 (see e. g. Refs. [39, 46, 47, 49, 50, 54–56] and references therein for detail). The atomic form-factor can be represented as the nuclear form-factor that takes into account the screening of the nucleus by Coulomb field due to the atomic electrons. Indeed, in the limit $t \rightarrow 0$ nuclear form-factor tends to $F_{nucl}(t) \rightarrow 1$ in opposite to the atomic form-factor, which tends to $F_{atom}(t) \rightarrow 0$ as $t \rightarrow 0$. In addition, screening charge density of the atomic form-factor can be represented as a convolution of the nuclear charge density with the specific screening density. In particular, following L. Schiff [57] to obtain the atomic form-factor one should multiply the nuclear form-factor by the screening term $t/(t_a + t)$.

First, let us consider the elastic atomic form-factor that was studied by Y. Tsai [49] and L. Schiff [58] in the following form [50]:

$$F_{TS}(t) = \frac{t}{(t_a + t)} \frac{1}{(1 + t/t_d)}, \quad (21)$$

where $\sqrt{t_a} = 1/R_a$ is a momentum transfer associated with nucleus Coulomb field screening due to the atomic electrons, with R_a being a typical magnitude of the atomic radius $R_a = 111Z^{-1/3}/m_e$, $\sqrt{t_d} = 1/R_n$ is the typical momentum associated with nuclear radius R_n , such that $R_n \simeq 1/\sqrt{d}$ and $d = 0.164A^{-2/3}\text{GeV}^2$. Since the integration with respect to t in Eq. (4) is dominated by $t \gtrsim t_{min}$, therefore the magnitude of t_{min} (see e. g. Eq. (11)) defines the typical form-factor approach to be considered. In particular, if $t_{min}/t_a \ll 1$, then the complete screening regime takes place, which implies that nucleus transfer momentum is small and the typical atomic elastic form-factor is much less than unity, $F_{TS}(t) \simeq t/t_a \ll 1$. On the other hand, as soon as $t_{min}/t_a \gg 1$, then no screening regime occurs. In this case the atomic elastic form-factor is scaled as $F_{TS}(t) \simeq 1/(1 + t/t_d)$ and the nucleus size effects dominate, it implies also that the typical nucleus transfer momentum squared is relatively large, $t_d \gg t_a$. It is worth noting, given the parameter space of interest $1\text{ MeV} \lesssim m_G \lesssim 1\text{ GeV}$ and $10\text{ GeV} \lesssim E_l \lesssim 100\text{ GeV}$ both screening and nucleus size parameters can contribute to the virtual photon flux and thus to the total yield of the G -boson production.

Next, let us consider the nuclear Helm's form-factor $F_{Hnucl}(t)$ that corresponds to the inverse Fourier transformation of the nucleus charge density $\rho(\vec{r})$. The latter can be represented as the convolution of the spherically

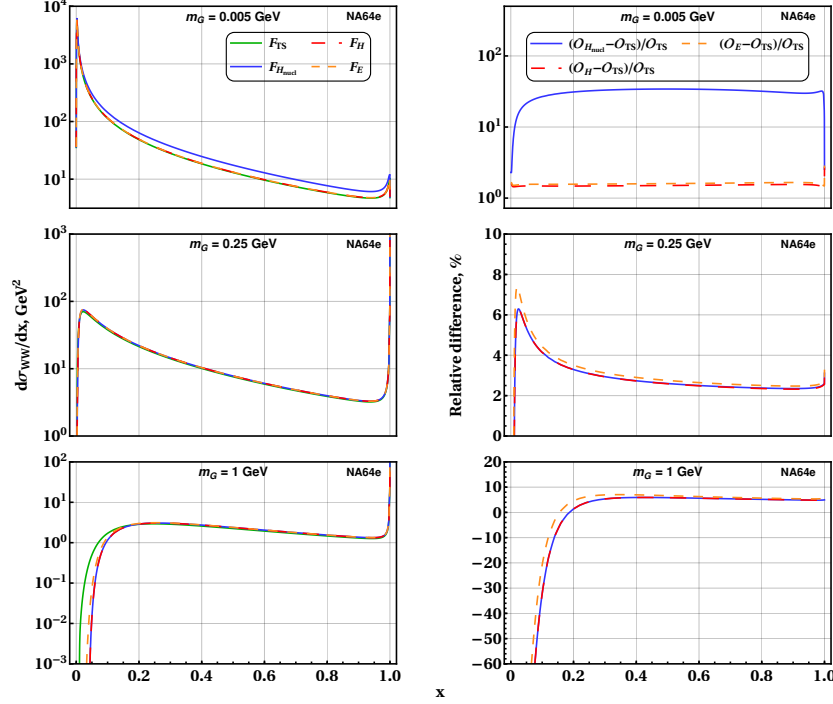


Figure 3. Left panel: the differential cross-section of a G -boson production at NA64e experiment as function of the energy fraction for the set of its mass and the set of form-factors. The set of masses is chosen to be: $m_G = 5$ MeV, $m_G = 250$ MeV and $m_G = 1$ GeV. The cross-section for F_{TS} is shown by the green solid line, the cross-section for $F_{H_{nucl}}$ is shown by blue solid line, the cross-section for F_H is shown by the red dashed line, the cross-section for F_E is shown by the orange dashed line. Right panel: the regarding relative differences of the the cross-sections for various form-factor parametrizations are expressed as $(\mathcal{O}_{H_{nucl}} - \mathcal{O}_{TS})/\mathcal{O}_{TS}$, $(\mathcal{O}_H - \mathcal{O}_{TS})/\mathcal{O}_{TS}$ and $(\mathcal{O}_E - \mathcal{O}_{TS})/\mathcal{O}_{TS}$ respectively, where $\mathcal{O} \equiv d\sigma/dx$.

uniform charge inside the nucleus and the Gaussian profile implying better accounting of the the edge of nucleus [59]. Both the nuclear Helm's form-factor $F_{H_{nucl}}(t)$ and atomic Helm's form-factor $F_H(t)$ read as follows respectively [60, 61]:

$$F_{H_{nucl}}(t) = \frac{3j_1(\sqrt{t}R_H)}{\sqrt{t}R_H} \exp\{-s_H^2 t/2\}, \quad (22)$$

$$F_H(t) = t/(t_a + t) F_{H_{nucl}}(t), \quad (23)$$

where $j_1(x)$ - first spherical Bessel function of the first kind, the effective nuclear radius R_H can be parameterized as

$$R_H = \sqrt{c_H^2 + 7/3\pi^2 a_H^2 - 5s_H^2},$$

where $s_H = 0.9$ fm is the nuclear shell thickness, $a_H = 0.52$ fm and $c_H = (1.23A^{1/3} - 0.6)$ fm. It is worth noting that we also set $F_{H_{nucl}}$ to zero for $t \gtrsim (4.49/R_H)^2$, it implies that we consider only non-negative values of the Helm's form-factor, since it vanishes at $t \simeq (4.49/R_H)^2$ and the dominant contribution for the photon flux is due to the typical range $t \lesssim (4.49/R_H)^2$ (for details see e. g. Ref. [61]).

Finlay, let us consider now the exponential atomic form-factor corresponding Gaussian charge distribution

that reads as follows [62]:

$$F_E(t) = t/(t_a + t) \exp(-tR_{exp}^2/6), \quad (24)$$

where the mean radius of nucleus is defined as $R_{exp} = (0.91A^{1/3} + 0.3)$ fm. As was discussed above, the screening term $t/(t_a + t)$ in Eq. (24) is introduced to take into account the shielding of the nucleus Coulomb field due to the atomic electrons.

Note that the general virtual photon flux (4) depends on both fraction of energy x and emission angle of spin-2 boson θ_G through the function of the lower limit $t_{min}(x, \theta_G)$ (see e. g. Eq. (11) for detail). So that it is instructive to study the the dependence of χ upon t_{min} for various form-factor parametrizations. Intriguingly, that the integration over dt in the virtual photon flux (4) of the Tsai-Schiff's elastic form-factor (21) can be performed in the analytical way through the elementary functions. The latter simplification can be exploited for the reducing of the computational time of χ_{TS} integration. As the result, the virtual photon flux in analytic form for

Tsai-Schiff's form-factor reads as follows:

$$\chi_{TS} = \frac{Z^2 t_d^2}{(t_a - t_d)^3} \left([C_1^\chi + C_2^\chi t_{min}] + [C_3^\chi + C_4^\chi t_{min}] \ln \left[\frac{t_{min} + t_d}{t_{min} + t_a} \right] \right) \quad (25)$$

where the functions C_1^χ , C_2^χ , C_3^χ and C_4^χ are defined by the following expressions respectively:

$$C_1^\chi = \left(\frac{t_d(t_a - t_d)}{t_d + t_{max}} + \frac{t_a(t_a - t_d)}{t_a + t_{max}} - \right. \quad (26)$$

$$\left. - 2(t_a - t_d) + (t_a + t_d) \ln \left[\frac{(t_d + t_{max})}{(t_a + t_{max})} \right] \right), \quad (27)$$

$$C_2^\chi = \left(\frac{t_a - t_d}{t_d + t_{max}} + \frac{t_a - t_d}{t_a + t_{max}} + 2 \ln \left[\frac{t_d + t_{max}}{t_a + t_{max}} \right] \right), \quad (28)$$

$$C_3^\chi = -(t_a + t_d), \quad C_4^\chi = -2. \quad (29)$$

The regarding flux for and exponential form-factor can be expressed through the special function as follows

$$\chi_E = Z^2 \left(\frac{t_a + t_{min}}{t + t_a} e^{-R_{exp}^2 t/3} + \frac{3 + R_{exp}^2(t_a + t_{min})}{3} e^{R_{exp}^2 t_a/3} \text{Ei} \left[-\frac{R_{exp}^2(t + t_a)}{3} \right] \right) \Big|_{t_{min}}^{t_{max}}, \quad (30)$$

where $\text{Ei}(x) = \int_{-\infty}^x e^t/t dt$ is the exponential integral function. Contrary, photon flux with Helm's form-factor cannot be integrated over t in analytical way, in what follows we perform the numerical integration for both χ_H and $\chi_{H_{nuc}}$. In addition, the numerical calculations reveal that general photon flux (4) depends weakly on t_{max} as long as $t_{max} \gg t_{min}, t_a, t_d$. On the other hand, one can show that the typical values of the t_{min}, t_a and t_d don't exceed the magnitude of the order of $\lesssim \mathcal{O}(1) \text{ GeV}^2$. In what follows we set $t_{max} \simeq 10 \text{ GeV}^2$ for the numerical estimations.

In the left panel of Fig. 2 we show the virtual photon fluxes χ as a functions of t_{min} for the lead target material of the NA64e experiment with atomic number of $Z = 82$ and particle number of $A = 207$ that parameterize both typical screening and nuclear radius. In the right panel of Fig. 2 we choose χ_{TS} as a benchmark photon flux and show the relative differences between it and the set of χ_E , χ_H and $\chi_{H_{nuc}}$. For the wide range of the typical momentum squared $10^{-10} \text{ GeV}^2 \lesssim t_{min} \lesssim 10^{-3} \text{ GeV}^2$ all the atomic photon fluxes match with a reasonable accuracy at the level of $\lesssim 5\%$. In order to illustrate the impact of the screening effect we show both the nuclear and atomic Helm's photon fluxes in Fig. 2. In particular, for the screening region $t_{min} \lesssim t_a \simeq 10^{-9} \text{ GeV}^2$ the nucleus photon flux $\chi_{H_{nuc}}$ exceeds the atomic one χ_H by 10% approximately. The latter one is associated also with the smaller slope of χ_H in the screening range $t_{min} \lesssim t_a$.

It is worth noting, that there are also form-factor models that consider the charge density as the sum of Gaussian, Fourier-Bessel functions and Klein-Nystrand's charge density [63–67]. In addition, the Fermi distribution for the nucleus charge is also discussed in the literature [60, 66]. We note that these nucleus form-factor parametrizations are beyond the scope of the present paper, even though we would expect that they provide a similar results for the flux shown in Fig. 2.

IV. MISSING ENERGY SIGNAL

In this section we discuss the setups for the fixed target experiments such as NA64e (SPS, CERN) [25–37, 68], LDMX (Fermilab) [40–43], NA64 μ (SPS, CERN) [38, 39] and M³ (Fermilab) [44, 45], that can potentially probe invisible decay of $G \rightarrow \chi\bar{\chi}$ in the associated charged lepton missing energy process $lN \rightarrow lNG(\rightarrow \chi\bar{\chi})$, where the label $l = (e, \mu)$ denotes either electron or muon beam and N denotes the nucleus of the target. Given the benchmark coupling Eq. (1), the spin-2 Dark Matter mediator G can decay through the different channels. In particular, as soon as $m_G \gtrsim 2m_l$ the visible decay $G \rightarrow l^+l^-$ is allowed with a specific decay width [9]

$$\Gamma(G \rightarrow l^+l^-) = \frac{c_l^2 m_G}{160\pi} \left(\frac{m_G}{\Lambda} \right)^2 \times (1 - 4m_l^2/m_G^2)^{3/2} (1 + 8m_l^2/(3m_G^2)), \quad (31)$$

where m_l is the mass of the charged lepton. The Lagrangian (1) also implies that for $m_G \gtrsim 2m_\chi$ the invisible decay into fermion DM pair $G \rightarrow \chi\bar{\chi}$ is kinetically allowed with a decay width

$$\Gamma(G \rightarrow \chi\bar{\chi}) = \frac{c_\chi^2 m_G}{160\pi} \left(\frac{m_G}{\Lambda} \right)^2 \times (1 - 4m_\chi^2/m_G^2)^{3/2} (1 + 8m_\chi^2/(3m_G^2)), \quad (32)$$

where m_χ is the mass of the hidden Dirac DM fermion. In this paper we focus on the processes of the invisible channel of G -boson decay into pair of hidden dark fermions, $G \rightarrow \chi\bar{\chi}$ with $\text{Br}(G \rightarrow \chi\bar{\chi}) \simeq 1$ for the sufficiently light DM particles, $m_G \gtrsim 2m_\chi$. It implies that decay widths obey the condition $\Gamma_{G \rightarrow \chi\bar{\chi}} \gg \Gamma_{G \rightarrow l^+l^-}$ and therefore the coupling constants are chosen to be $c_\chi \gg c_l$ for the parameter space of interest $1 \text{ MeV} \lesssim m_G \lesssim 1 \text{ GeV}$. As the result, this benchmark conditions imply the rapid decay of spin-2 DM mediator to $\chi\bar{\chi}$ pair after its production in the process $lN \rightarrow lNG$.

Let us estimate N_G the number of G produced by the lepton beam at fixed target as follows

$$N_G \simeq \text{LOT} \cdot \frac{\rho N_A}{A} L_T \int_{x_{min}}^{x_{max}} dx \frac{d\sigma_{2 \rightarrow 3}(E_l)}{dx} \text{Br}(G \rightarrow \chi\bar{\chi}), \quad (33)$$

where LOT is number of leptons accumulated on target, ρ is target density, N_A is Avogadro's number, A

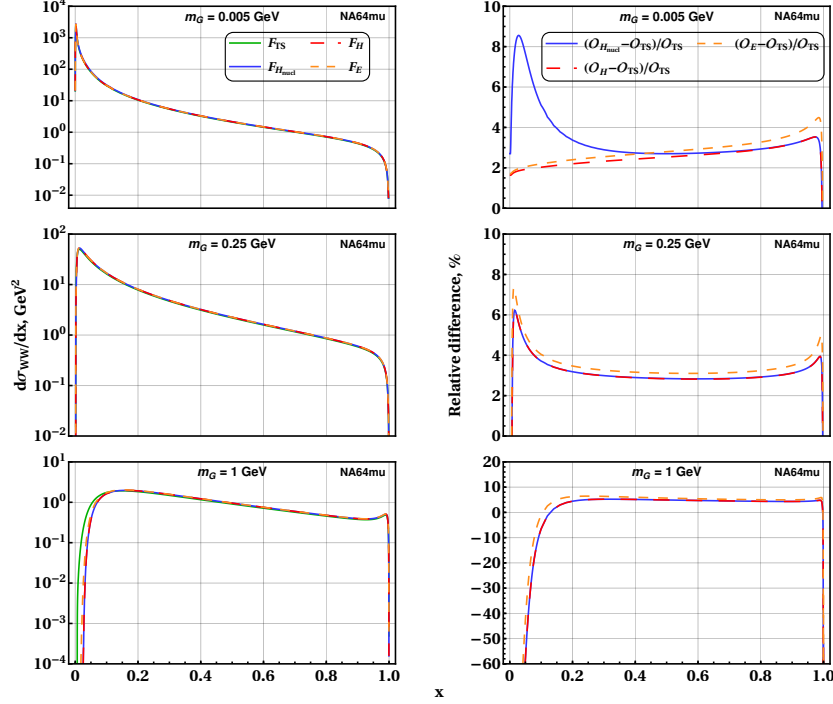


Figure 5. Same as in Fig. 3 but for the NA64μ experiment.

B. LDMX

The Light Dark Matter Experiment (LDMX) is the projected electron fixed-target facility at Fermilab, that aims probing the relic DM particles in the mass range between 1 MeV and 1 GeV. It can be considered as a facility that is complimentary to NA64e experiment due to its unique electron missing momentum technique [69]. It is remarkable that the missing-energy cuts and active veto system of both NA64e and LDMX experiments provide a significant background suppression at the level of $\lesssim 10^{-12}$.

The projected LDMX experiment would employ the target, the silicon tracker and both the hadron and electromagnetic calorimeter. The lost of the primary electron beam energy can be associated with G -boson emission in the thin upstream target of the LDMX. The regarding missing momentum of the electron can be measured by the silicon tracker system, electromagnetic and hadron calorimeter which are located downstream. The missing energy cut of the recoil electron is set to be $E_e^{rec} \lesssim 0.3E_e$, that implies $x_{min} = 0.7$ in Eq. (33). We perform the analysis of the LDMX sensitivity for aluminium target (Al) ($\rho = 2.7 \text{ g cm}^{-3}$, $A = 27 \text{ g mole}^{-1}$, $Z = 13$) with a thickness of $L_T \simeq 0.4X_0 \simeq 3.56 \text{ cm}$, where $X_0 = 8.9 \text{ cm}$ is a radiation length of the electron in the aluminium. The energy of the beam is chosen to be $E_e \simeq 16 \text{ GeV}$ and the projected statistics corresponds to EOT $\simeq 10^{16}$ for the final phase of experimental running after 2027 (see e. g. Ref. [43] and references therein for detail).

C. NA64μ

The NA64μ experiment is the fixed-target facility at the CERN SPS that searches for the dark sector particles in the muon beam missing momentum mode $\mu N \rightarrow \mu NG$. It can be considered as a complementary experiment to NA64e. For the sensitivity estimation of NA64μ we set the energy of the muon beam to be $E_\mu \simeq 160 \text{ GeV}$ and choose MOT $\simeq 5 \times 10^{13}$ as the projected statistics for the muons accumulated on target. The NA64μ experiment employs the lead Shashlyk-type electromagnetic calorimeter that serves as a target with a thickness of $L_T \simeq 40X_0 \simeq 22.5 \text{ cm}$. We note that one can neglect the muon stopping loss in the lead target of $\simeq 22.5 \text{ cm}$ for the ultra-relativistic muons of $E_\mu \simeq 160 \text{ GeV}$ due to small energy attenuation in the lead $\langle dE_\mu/dx \rangle \simeq 12.7 \times 10^{-3} \text{ GeV/cm}$ (see e. g. Ref. [70] for detail).

In order to measure the momentum of incident and outgoing muon, the NA64μ facility employs two magnet spectrometers. We choose the typical cut for the outgoing muon as $E_\mu^{rec} \lesssim 0.5E_\mu \simeq 80 \text{ GeV}$, that corresponds to $x_{min} = 0.5$ in Eq. (33). We note that for NA64μ facility approximately $\simeq 120$ days are needed to accumulate statistics of MOT $\simeq 5 \times 10^{13}$ relative to EOT $\simeq 5 \times 10^{12}$ for NA64e facility. This can be explained by the increased intensity of muon beam line at M3 that is higher by factor of $\simeq 10$ than the intensity of electron beam at H4.

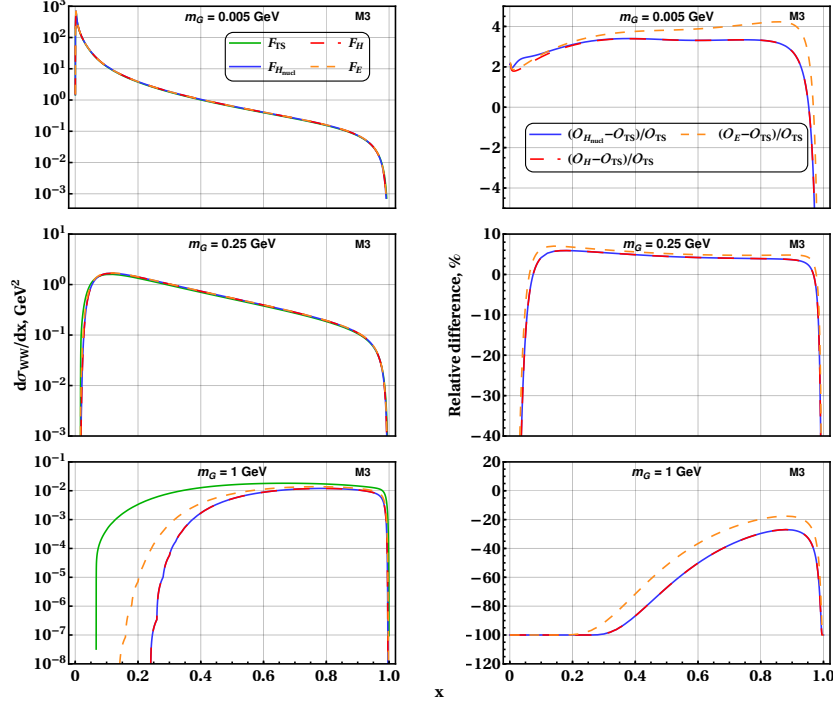


Figure 6. Same as in Fig. 3 but for the M^3 experiment.

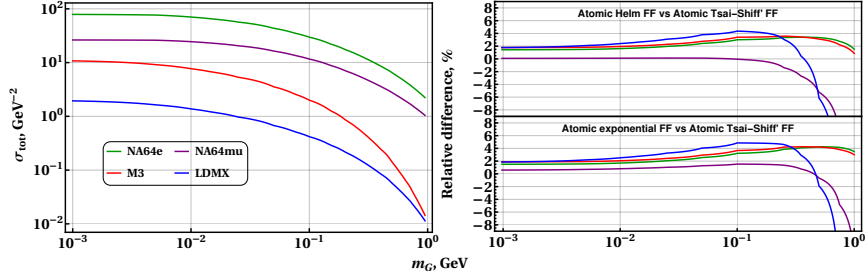


Figure 7. Left panel: total cross section of G -boson production as function of its mass for the set of experiments associated with benchmark Tsai-Shiff's form-factor. We set here $c_l/\Lambda = 1 \text{ GeV}^{-1}$ and integrate the cross-section over specific experimental cut range, $x_{min} \lesssim x \lesssim x_{max}$ (see text for detail). Right panel: the relative difference is expressed as $(\mathcal{O}_H - \mathcal{O}_{TS})/\mathcal{O}_{TS}$ (right upper) and $(\mathcal{O}_E - \mathcal{O}_{TS})/\mathcal{O}_{TS}$ (right bottom) for atomic Helm's and the exponential form-factors respectively, where $\mathcal{O} = \sigma_{tot}$. The green line corresponds to the NA64e facility, the violet line is associated with the NA64 μ experiment, the red line corresponds to the M^3 facility, the blue line is associated with the LDMX experiment.

D. M^3

The muon missing momentum experiment (M^3) at Fermilab is the projected fixed target facility that aims probing dark sector particles by employing the muon-specific missing energy signature $\mu N \rightarrow \mu N G (\rightarrow \chi \bar{\chi})$. It utilizes the muon beam of $E_\mu \simeq 15 \text{ GeV}$ impinging on the tungsten target (W) ($\rho = 19.3 \text{ g cm}^{-3}$, $A = 184 \text{ g mole}^{-1}$, $Z = 74$) of the typical thickness of $L_T \simeq 50 X_0 \simeq 17.5 \text{ cm}$, where $X_0 \simeq 0.35 \text{ cm}$ is the radiation length of electron in the tungsten. The regarding facility also exploits a downstream detector to veto the Standard model background. It aims to collect MOT $\simeq 10^3$

during $\simeq 3$ months of the experimental running. The cut on the missing momentum of muon is chosen to be $E_\mu^{rec} \lesssim 9 \text{ GeV}$, this yields the lower limit on the energy fraction $x_{min} \simeq 0.4$ in Eq. (33).

To conclude this subsection we note that for muons of $E_\mu \simeq 15 \text{ GeV}$ the muon stopping loss in the tungsten [45] is estimated to be of the order of 530 MeV through the target medium of $50 X_0$. This allows one to neglect $\langle dE_\mu/dx \rangle$ in the numerical calculation of the yield of G -boson at M^3 . As a result that justifies the exploiting of Eq. (33) for the estimate of N_G with $L_T \simeq 50 X_0$ at M^3 facility.

V. THE DIFFERENTIAL AND TOTAL CROSS SECTIONS

In this section we study both the single-differential and total cross sections in the WW approximation for the set of the form-factors discussed in Section III. The results are presented for the benchmark parameters of the lepton fixed target experiments which can potentially probe the invisible signatures associated with a lepton missing energy in bremsstrahlung-like process $lN \rightarrow lNG(\rightarrow \chi\bar{\chi})$. The total σ_{tot} cross-sections are obtained by the numerical integration of the double-differential cross section (6) for the specific experimental cuts. In the left panels of Figs. 3, 4, 5, and 6 we show the differential cross-sections of G -boson production as function of energy fraction $x = E_G/E_l$ for the NA64e, LDMX, NA64 μ and M³ experiments respectively and for the set of form-factors discussed in Sec. III. These cross-sections are also presented for the specific set of G -boson masses, $m_G = 5$ MeV, $m_G = 250$ MeV and $m_G = 1$ GeV.

Let us describe now the typical properties and the general kinematics of G -boson production by the charged lepton beams impinging on the solid target. It is worth mentioning that both NA64e and LDMX electron cross-sections have a peak in the region $x \lesssim 1$ for the relatively heavy masses $m_G \gtrsim 250$ MeV, it means that the signal of G -boson production is strongly forward peak, such that the dominant part of the initial beam energy transfers to the hidden spin-2 boson. On the other hand, for the relatively light masses $m_G \lesssim 5$ MeV the sharp forward peak is mitigated and the regarding differential cross-section is in the soft bremsstrahlung-like regime. It implies that the cross-section peaks in the infra-red (IR) region $x = E_G/E_e \ll 1$. However, for the higher masses $m_G \gtrsim 250$ MeV the IR peak is smeared as long as the energy fraction is small.

Remarkably that both NA64 μ and M³ muon cross-sections are in the soft bremsstrahlung-like regime $d\sigma_\mu/dx \propto \mathcal{O}(1/x)$ as long as $x \ll 1$ for all masses in the range $1 \text{ MeV} \lesssim m_G \lesssim 1 \text{ GeV}$, since the mass of spin-2 boson is comparable to the muon mass in that region, $m_G \propto \mathcal{O}(m_\mu)$.

Let us describe now the impact of various form-factor parametrizations on the shape of the differential cross-sections. In order to compare these cross-sections we choose Tsai-Shiff's form-factor as a benchmark one, since the latter is exploited widely in the calculations of WW cross-section for both beam dump and fixed target experiments (see e. g. Refs. [39, 45, 50, 70] and references therein for detail). In what follows in the right panels of Figs. 3, 4, 5, and 6 we show the relative differences between $(d\sigma/dx)_{TS}$ and the set of $(d\sigma/dx)_{H_{nuc}}$, $(d\sigma/dx)_H$ and $(d\sigma/dx)_E$ respectively for the specific experiments and the specific masses of G -boson. We recall again for clarity, that the subscriptions of $F_{TS}(t)$, $F_H(t)$ and $F_E(t)$ are related to the atomic elastic form-factors with screening term, while the label of $F_{H_{nuc}}(t)$ is associated with the nuclear elastic form-factor that doesn't take into ac-

count the screening effect.

It is worth mentioning that given the mass m_G all the atomic form-factor cross-sections for the NA64e experiment match with a reasonable accuracy at the level of 2% – 10% as soon as $0.2 \lesssim x \lesssim 1$. However, the sizable deviation (i. e. at the level of $\propto \mathcal{O}(2)$) between the nuclear and atomic cross-sections appears only for the small mass region long as $m_G \lesssim 5$ MeV. These effects are shown in the right panel of Fig. 3. The regarding impact of the form-factor parametrization on the differential cross-section shape is shown in the right panel of Fig. 4 for the LDMX electron fixed-target experiment. In addition we note that the shapes of the cross-sections can be varied for $x \ll 1$ and $m_G \lesssim 1$ GeV, however this energy fraction region doesn't provide a sizeable contribution to the total cross-section of heavy masses.

For the muon beam cross-sections of the NA64 μ experiment the impact of the different form-factor parametrization can be estimated at the level of $\lesssim 2\%$ –8% for energy fraction in the range $0.2 \lesssim x \lesssim 1$. The latter is shown in the right panel of Fig. 5. One can see also from Fig. 6 that the shape of the differential cross-section for the M³ experiment can be varied significantly due to the form-factors as long as $x \ll 1$ and $m_G \lesssim 1$ GeV.

Let us study now the specific shape of the total cross-sections of G -boson production. In the left panel of Fig. 7 we show the regarding cross-sections for the NA64e, LDMX, NA64 μ and M³ facilities, which are calculated for the benchmark Tsai-Shiff's atomic elastic form-factor. One can see from Fig. 7 that both NA64e and NA64 μ cross-sections are calculated for the lead (Pb) target ($Z \simeq 82$), nevertheless the the total electron beam cross-section σ_e^{tot} is generally larger by factor of $\simeq 5$ than the muon beam cross-section σ_μ^{tot} , even though they have a comparable energies of the impinging beams $E_e \simeq E_\mu \simeq \mathcal{O}(100)$ GeV. That implies the advantage of using the electron beam instead of muon beam at the CERN SPS facility in the mass range $1 \text{ MeV} \lesssim m_G \lesssim 1 \text{ GeV}$. However, if one compares the LDMX electron cross-section for the aluminium (Al) target ($Z \simeq 13$) with the M³ cross-section for the muon beam impinging on the tungsten (W) target ($Z \simeq 74$), one can conclude that the regarding advantage of using the electron beam is compensated by the nucleus charge suppression $\simeq 13/74$, even though both LDMX and M³ experiments have a comparable beam energies, $E_\mu \simeq E_e \simeq 15$ GeV. In addition we note from the NA64 μ and M³ cross-sections that the greater energy of the muon beam implies greater rate of the G -boson production, $\sigma_\mu^{tot}(160 \text{ GeV}) \gtrsim \sigma_e^{tot}(16 \text{ GeV})$. To conclude this section, we specify briefly the impact of the form-factor parametrization on the total cross-section. In the right panel of Fig. 7 the relative differences of the total cross-sections are shown for the set of atomic form-factors. In the small mass region $m_G \lesssim 100$ MeV these differences are relatively small, i. e. at the level of $\lesssim 2\%$. However, the regarding discrepancies can be as large as $\gtrsim 8\%$ for the heavy mass region $m_G \lesssim 1$ GeV.

VI. THE EXPERIMENTAL LIMITS

In this section we study current and expected reach of the lepton fixed-target experiments. The limit on the coupling c_l/Λ can be obtained as follows. By exploiting both Eq. (33) for the number of produced G -bosons and the result on its production cross-section with specific experimental cuts, one can require that the number of signal events is $N_G \gtrsim 2.3$. As a result, this yields 90% C.L. exclusion limit on the coupling constant c_l/Λ for the background free case and null result of the fixed-target facilities. In the left panel of Fig. 8 we show by the dashed lines the projected sensitivities of NA64e, LDMX, NA64 μ and M³ fixed target facilities.

It is worth mentioning that the expected reach of the LDMX is rather strong, i. e. at the level of $c_l/\Lambda \gtrsim 10^{-5} \text{ GeV}^{-1}$, even though the typical cross-section of the G -boson production is fairly small (see e. g. the blue line in the left panel of Fig. 7). The enhanced expected reach of the LDMX is associated with fairly large number of the electrons that will be accumulated on target. In particular, by the final phase of data taking LDMX plans to accumulate EOT $\simeq 10^{16}$, as we discussed it above in Sec. IV B.

In addition, from the projected sensitivities of both NA64 μ and M³ muon experiments shown in Fig. 8, one can conclude that compared to the M³ option with 16 GeV beam muons and MOT $\simeq 10^{13}$, the higher energy muons of NA64 μ (e. g. $E_\mu \simeq 160 \text{ GeV}$) with MOT $\simeq 5 \times 10^{13}$ allow examining a wider region in the parameter space of the spin-2 boson scenario. Nevertheless, the ultimate projected bounds of the NA64e experiment for EOT $\simeq 5 \times 10^{12}$ (see e. g. the green dashed line in the left panel of Fig. 8 at the level of $c_l/\Lambda \gtrsim 10^{-4} \text{ GeV}^{-1}$), can be ruled out even by the M³ facility at the level of $c_l/\Lambda \gtrsim 7 \times 10^{-5} \text{ GeV}^{-1}$ (see e. g. the red dashed line in the left panel of Fig. 8). In the left panel of Fig. 8, we show by the solid green line the excluded limit of the NA64e experiment (at the level of $c_l/\Lambda \gtrsim 7 \times 10^{-4} \text{ GeV}^{-1}$) for the current accumulated statistics of EOT $\simeq 3.22 \times 10^{11}$. In particular, from the analysis of the NA64e data collected during 2016-2021 runs no signal events were found for the background free case (see e. g. Ref. [32]), as we discussed it in Sec. IV A.

It is worth mentioning that authors of Ref. [10] have been already considered the bounds on the light spin-2 mediator from $e^+e^- \rightarrow \gamma + E_{\text{miss}}$ at BaBar experiment [71]. The analysis was carried out for mainly invisible decay mode $\text{Br}(G \rightarrow \chi\bar{\chi}) \simeq 1$. The regarding exclusion limit yields the magnitude of the coupling constant at the level of $c_e/\Lambda \gtrsim 2 \times 10^{-4} \text{ GeV}^{-1}$ for the masses in the range $1 \text{ MeV} \lesssim m_G \lesssim 1 \text{ GeV}$. These bounds are shown by the solid black line in the left panel of Fig. 8. One can conclude that it rules out the current experimental constraints of the NA64e facility for EOT $\simeq 3.22 \times 10^{11}$.

To conclude this section, we discuss briefly the impact of the form-factor parametrization on the experimental

limits c_l/Λ for the fixed target facilities. In the right panel of Fig. 8 the relative differences of the coupling constants are shown for the set of atomic form-factors. In the small mass region $m_G \lesssim 100 \text{ MeV}$ these differences are relatively small, i. e. at the level of $\lesssim 2\%$. However, the regarding discrepancies can be as large as $\gtrsim 8\%$ for the heavy mass region $m_G \lesssim 1 \text{ GeV}$.

VII. CONCLUSION

In the present paper we have discussed in detail the probing of the massive spin-2 boson G through its invisible decay into pair of DM particles χ with $\text{Br}(G \rightarrow \chi\bar{\chi}) \simeq 1$. The regarding scenario implies that the G -boson serves as a mediator between charged leptons of SM and DM sector. The benchmark simplified coupling of this model involves the dimension-5 operators of massive $G_{\mu\nu}$ field and the energy momentum tensors of both SM and DM particles. We have studied explicitly the missing energy signatures for the projected and existing lepton fixed-target experiments, such as NA64e, LDMX, NA64 μ and M³. Namely, by exploiting the WW approach, we have calculated G -boson production cross-section in the process $lN \rightarrow lNG$ followed by its invisible decay into DM particles $G \rightarrow \chi\bar{\chi}$ for the specific fixed-target experiments. We have calculated the expected reach for the regarding experiments, implying the background free case and null result for DM detection. Moreover, we have also discussed in detail the impact of both nuclear and atomic form-factor parametrizations on (i) the differential spectra of G boson emission, (ii) the total cross-section of its production (iii) the experimental reach of the fixed-target facilities for probing hidden spin-2 boson. It was found that the total yield of spin-2 boson production and the regarding experimental reach can be affected by the form-factor at the level of $\simeq 8\% - 10\%$ for the large mass region $m \lesssim 1 \text{ GeV}$. For the light masses of G -boson, $m_G \lesssim 100 \text{ MeV}$, the implication of the form-factors for the yield and experimental reach is estimated at the level of $\lesssim 2\%$.

ACKNOWLEDGMENTS

We would like to thank P. Crivelli, S. Demidov, S. Gninenko, D. Gorbunov, M. Kirsanov, N. Krasnikov, V. Lyubovitskij, L. Molina Bueno, A. Pukhov, H. Sieber and A. Zhevlakov for very helpful discussions and correspondences. The work of D. V. K on description of the dark matter missing energy signatures of NA64e and regarding exclusion limits for spin-2 DM mediator is supported by the Russian Science Foundation RSF grant 21-12-00379.

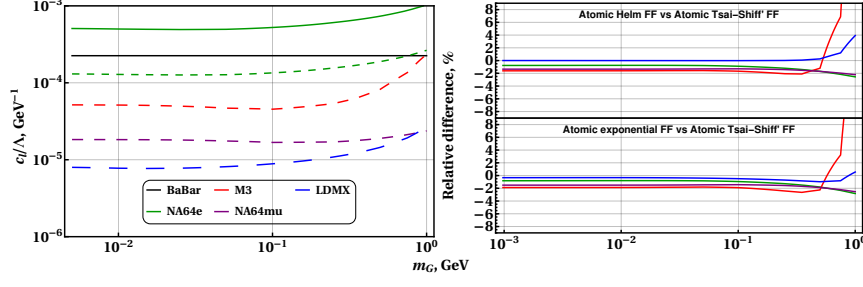


Figure 8. Left panel: 90 % $C.L.$ limits on c_l/Λ coupling constant for the fixed-target and BaBar experiment [10] as a function of G -boson mass m_G . For all expected reaches, we imply that $\text{Br}(G \rightarrow \chi\bar{\chi}) \simeq 1$ and $m_G \gtrsim 2m_\chi$. In addition, in the left panel all curves for the fixed-target facilities imply the Tsai-Shiff's form-factor in the cross-section. The green dashed line is the projected sensitivity of the NA64e experiment for EOT $\simeq 5 \times 10^{12}$, the red dashed line is the expected reach of the M³ facility for MOT $\simeq 10^{13}$, the violet dashed line is the projected sensitivity of the NA64 μ experiment for MOT $\simeq 5 \times 10^{13}$ and the blue dashed line is the expected reach of the LDMX facility for EOT $\simeq 10^{16}$. The green solid line represents the excluded at 90 % $C.L.$ bound of the NA64e experiment for EOT $\simeq 3.22 \times 10^{11}$. Right panel: the relative difference is expressed as $(\mathcal{O}_H - \mathcal{O}_{TS})/\mathcal{O}_{TS}$ (right upper) and $(\mathcal{O}_E - \mathcal{O}_{TS})/\mathcal{O}_{TS}$ (right bottom) for atomic Helm's and the exponential form-factors respectively, where $\mathcal{O} = c_l/\Lambda$.

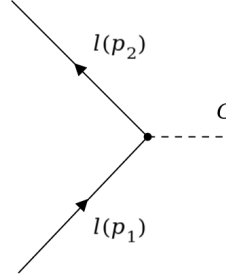
Appendix A: Matrix element for process $l^- \gamma \rightarrow Gl^-$

In this section, we collect an expressions for the Feynman diagrams [9, 72] associated with spin-2 boson production and the matrix element squared for process $l^- \gamma \rightarrow Gl^-$. In particular, we use the expression for

polarization sum of spin-2 mediator:

$$\sum_s e_{\mu\nu}(k, s) e_{\alpha\beta}(k, s) = 1/2(P_{\alpha\mu}P_{\beta\nu} + P_{\beta\mu}P_{\alpha\nu} - 2/3 P_{\mu\nu}P_{\alpha\beta}), \quad (\text{A1})$$

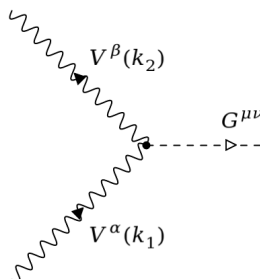
where $P_{\mu\nu} = g_{\mu\nu} - \frac{k_\mu k_\nu}{m_G^2}$. The vertex for the outgoing G -boson in case of incoming $l(p_1)$ and outgoing $l(p_2)$ leptons is



$$G^{\mu\nu} = -\frac{ic_l}{4\Lambda} \{ (p_2 + p_1)^\mu \gamma^\nu + (p_2 + p_1)^\nu \gamma^\mu - 2g^{\mu\nu}(p_2^\mu + p_1^\mu - 2m_l) \}. \quad (\text{A2})$$

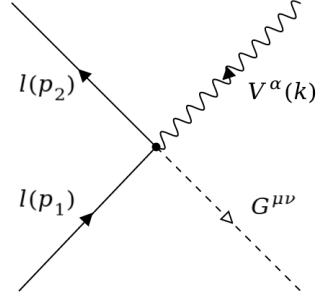
For the incoming $V^\alpha(k_1)$ and outgoing $V^\beta(k_2)$ massless

vector bosons one has



$$G^{\mu\nu} = -\frac{ic_\gamma}{\Lambda} \left\{ \eta^{\alpha\beta} k_1^\mu k_2^\nu + \eta^{\mu\alpha} ((k_1, k_2) \eta^{\nu\beta} - k_1^\beta k_2^\nu) - \eta^{\mu\beta} k_1^\nu k_2^\alpha + 1/2 \eta^{\mu\nu} (k_1^\beta k_2^\alpha - (k_1, k_2) \eta^{\alpha\beta}) + (\mu \longleftrightarrow \nu) \right\}. \quad (\text{A3})$$

Finally the vertex for 4-point interaction is



$$= \frac{c_l e}{2} (\eta^{\mu\alpha} \gamma^\nu + \eta^{\nu\alpha} \gamma^\mu). \quad (\text{A4})$$

As a result, by using FeynCalc package [51, 52] for the Wolfram Mathematica [53], we get matrix element squared for process $l^- \gamma \rightarrow l^- G$:

$$|\mathcal{M}_{l^- \gamma \rightarrow Gl^-}|^2 = \frac{c_l^2 e^2}{\Lambda^2} \frac{u_2 [s_2 - 2m_l^2] [(t_2 + u_2)^2 + (u_2 - m_G^2)^2] [4u_2 (2m_l^2 - s_2) - m_G^2 t_2]}{4t_2 (u_2 - m_l^2)^2 (s_2 - m_l^2)^2} - \frac{c_l^2 e^2}{\Lambda^2} \frac{m_l^2 R(m_l, m_G, t_2, u_2)}{12t_2^2 (m_l^2 - u_2)^2 (s_2 - m_l^2)^2}, \quad (\text{A5})$$

where $R(m_l, m_G, t, u)$ is regular expression for m_l and m_G :

$$\begin{aligned} R(m_l, m_G, t, u) = & 24m_l^{10}t + 24m_l^8[m_G^4 + 5m_G^2t - 6tu] + \\ & + 2m_l^6[24m_G^6 + 6m_G^4(15t - 8u) - 3m_G^2t(33t + 92u) + 2t(13t^2 + 18tu + 90u^2)] + \\ & + 2m_l^4[12m_G^8 + 12m_G^6(5t - 6u) + m_G^4(72u^2 - 113t^2 - 288tu) + \\ & + 4m_G^2t(t + 3u)(13t + 42u) - t(7t^3 + 64t^2u + 144tu^2 + 240u^3)] + \\ & + m_l^2[12m_G^8(3t - 4u) - 3m_G^6(29t^2 + 80tu - 48u^2) + m_G^4(70t^3 + 544t^2u + 696tu^2 - 96u^3) - \\ & - m_G^2t(27t^3 + 364t^2u + 852tu^2 + 912u^3) + 2t(t^4 + 46t^3u + 92t^2u^2 + 216tu^3 + 180u^4)] + \\ & + [-3m_G^8(3t^2 + 16tu - 8u^2) + m_G^6(15t^3 + 128t^2u + 168tu^2 - 48u^3) - \\ & - m_G^4(9t^4 + 122t^3u + 362t^2u^2 + 384tu^3 - 24u^4) + \\ & + m_G^2t(3t^4 + 68t^3u + 240t^2u^2 + 552tu^3 + 408u^4) - \\ & - 2tu(t + u)(7t^3 + 24t^2u + 72tu^2 + 72u^3)], \quad (\text{A6}) \end{aligned}$$

-
- | | |
|--|---|
| <p>[1] B. Holdom, Phys. Lett. B 166, 196 (1986).
 [2] L. B. Okun, Sov. Phys. JETP 56, 502 (1982).
 [3] C. Boehm and P. Fayet, Nucl. Phys. B 683, 219 (2004), arXiv:hep-ph/0305261.
 [4] M. Pospelov, A. Ritz, and M. B. Voloshin, Phys. Lett. B 662, 53 (2008), arXiv:0711.4866 [hep-ph].
 [5] J. McDonald, Phys. Rev. D 50, 3637 (1994), arXiv:hep-ph/0702143.
 [6] C. P. Burgess, M. Pospelov, and T. ter Veldhuis, Nucl. Phys. B 619, 709 (2001), arXiv:hep-ph/0011335.
 [7] J. D. Wells, Perspectives on LHC Physics, 283 (2008), arXiv:0803.1243 [hep-ph].
 [8] R. M. Schabinger and J. D. Wells, Phys. Rev. D 72, 093007 (2005), arXiv:hep-ph/0509209.
 [9] H. M. Lee, M. Park, and V. Sanz, Eur. Phys. J. C 74,</p> | <p>2715 (2014), arXiv:1306.4107 [hep-ph].
 [10] Y.-J. Kang and H. M. Lee, The European Physical Journal C 80 (2020), 10.1140/epjc/s10052-020-8153-x, arXiv:2001.04868.
 [11] M. G. Folgado, A. Donini, and N. Rius, JHEP 04, 036 (2020), arXiv:1912.02689 [hep-ph].
 [12] Y.-J. Kang and H. M. Lee, Eur. Phys. J. C 81, 868 (2021), arXiv:2002.12779 [hep-ph].
 [13] H. M. Lee, M. Park, and V. Sanz, JHEP 05, 063 (2014), arXiv:1401.5301 [hep-ph].
 [14] C. Han, H. M. Lee, M. Park, and V. Sanz, Phys. Lett. B 755, 371 (2016), arXiv:1512.06376 [hep-ph].
 [15] B. M. Dillon and V. Sanz, Phys. Rev. D 96, 035008 (2017), arXiv:1603.09550 [hep-ph].
 [16] B. M. Dillon, C. Han, H. M. Lee, and M. Park, Int.</p> |
|--|---|

- J. Mod. Phys. A **32**, 1745006 (2017), arXiv:1606.07171 [hep-ph].
- [17] A. Carrillo-Monte Verde, Y.-J. Kang, H. M. Lee, M. Park, and V. Sanz, JHEP **06**, 037 (2018), arXiv:1803.02144 [hep-ph].
- [18] S. Kraml, U. Laa, K. Mawatari, and K. Yamashita, Eur. Phys. J. C **77**, 326 (2017), arXiv:1701.07008 [hep-ph].
- [19] T. D. Rueter, T. G. Rizzo, and J. L. Hewett, JHEP **10**, 094 (2017), arXiv:1706.07540 [hep-ph].
- [20] M. G. Folgado, A. Donini, and N. Rius, (2019), 10.1007/JHEP01(2020)161, [Erratum: JHEP **02**, 129 (2022)], arXiv:1907.04340 [hep-ph].
- [21] N. Bernal, M. Dutra, Y. Mambrini, K. Olive, M. Peloso, and M. Pierre, Phys. Rev. D **97**, 115020 (2018), arXiv:1803.01866 [hep-ph].
- [22] Abi (Muon $g - 2$ Collaboration), Phys. Rev. Lett. **126**, 141801 (2021).
- [23] T. Aoyama, Physics Reports **887**, 1 (2020), the anomalous magnetic moment of the muon in the Standard Model.
- [24] D. Huang, C.-Q. Geng, and J. Wu, (2022), arXiv:2207.13421 [hep-ph].
- [25] S. N. Gninenko, N. V. Krasnikov, M. M. Kirsanov, and D. V. Kirpichnikov, Phys. Rev. D **94**, 095025 (2016), arXiv:1604.08432 [hep-ph].
- [26] D. Banerjee *et al.* (NA64), Phys. Rev. Lett. **118**, 011802 (2017), arXiv:1610.02988 [hep-ex].
- [27] D. Banerjee *et al.* (NA64), Phys. Rev. D **97**, 072002 (2018), arXiv:1710.00971 [hep-ex].
- [28] S. N. Gninenko, D. V. Kirpichnikov, and N. V. Krasnikov, Phys. Rev. D **100**, 035003 (2019), arXiv:1810.06856 [hep-ph].
- [29] D. Banerjee *et al.*, Phys. Rev. Lett. **123**, 121801 (2019), arXiv:1906.00176 [hep-ex].
- [30] R. R. Dusaev, D. V. Kirpichnikov, and M. M. Kirsanov, Phys. Rev. D **102**, 055018 (2020), arXiv:2004.04469 [hep-ph].
- [31] Y. M. Andreev *et al.*, Phys. Rev. D **104**, L091701 (2021), arXiv:2108.04195 [hep-ex].
- [32] Y. M. Andreev *et al.*, (2022), arXiv:2207.09979 [hep-ex].
- [33] Y. M. Andreev *et al.* (NA64), Phys. Rev. D **106**, 032015 (2022), arXiv:2206.03101 [hep-ex].
- [34] N. Arefyeva, S. Gninenko, D. Gorbunov, and D. Kirpichnikov, Phys. Rev. D **106**, 035029 (2022), arXiv:2204.03984 [hep-ph].
- [35] A. S. Zhevlakov, D. V. Kirpichnikov, and V. E. Lyubovitskij, Phys. Rev. D **106**, 035018 (2022), arXiv:2204.09978 [hep-ph].
- [36] C. Cazzaniga *et al.* (NA64), Eur. Phys. J. C **81**, 959 (2021), arXiv:2107.02021 [hep-ex].
- [37] Y. M. Andreev *et al.* (NA64), Phys. Rev. Lett. **126**, 211802 (2021), arXiv:2102.01885 [hep-ex].
- [38] H. Sieber, D. Banerjee, P. Crivelli, E. Depero, S. N. Gninenko, D. V. Kirpichnikov, M. M. Kirsanov, V. Poliakov, and L. M. Bueno, Phys. Rev. D **105**, 052006 (2022).
- [39] D. V. Kirpichnikov, H. Sieber, L. M. Bueno, P. Crivelli, and M. M. Kirsanov, Phys. Rev. D **104**, 076012 (2021), arXiv:2107.13297 [hep-ph].
- [40] A. Berlin, N. Blinov, G. Krnjaic, P. Schuster, and N. Toro, Phys. Rev. D **99**, 075001 (2019).
- [41] A. M. Ankowski, A. Friedland, S. W. Li, O. Moreno, P. Schuster, N. Toro, and N. Tran, Phys. Rev. D **101**, 053004 (2020), arXiv:1912.06140 [hep-ph].
- [42] P. Schuster, N. Toro, and K. Zhou, Phys. Rev. D **105**, 035036 (2022), arXiv:2112.02104 [hep-ph].
- [43] T. Åkesson *et al.*, in *2022 Snowmass Summer Study* (2022) arXiv:2203.08192 [hep-ex].
- [44] R. Capdevilla, D. Curtin, Y. Kahn, and G. Krnjaic, JHEP **04**, 129 (2022), arXiv:2112.08377 [hep-ph].
- [45] Y. Kahn, G. Krnjaic, N. Tran, and A. Whitbeck, JHEP **09**, 153 (2018), arXiv:1804.03144 [hep-ph].
- [46] Y.-S. Liu, D. McKeen, and G. A. Miller, Phys. Rev. D **95**, 036010 (2017).
- [47] Y.-S. Liu and G. A. Miller, Phys. Rev. D **96**, 016004 (2017).
- [48] K. J. Kim and Y.-S. Tsai, Phys. Rev. D **8**, 3109 (1973).
- [49] Y.-S. Tsai, Rev. Mod. Phys. **46**, 815 (1974).
- [50] J. D. Bjorken, R. Essig, P. Schuster, and N. Toro, Phys. Rev. D **80**, 075018 (2009), arXiv:0906.0580.
- [51] V. Shtabovenko, R. Mertig, and F. Orellana, Comput. Phys. Commun. **207**, 432 (2016), arXiv:1601.01167 [hep-ph].
- [52] V. Shtabovenko, R. Mertig, and F. Orellana, Comput. Phys. Commun. **256**, 107478 (2020), arXiv:2001.04407 [hep-ph].
- [53] W. R. Inc., “Mathematica, Version 13.1,” Champaign, IL, 2022.
- [54] C. Perdrisat, V. Punjabi, and M. Vanderhaeghen, Progress in Particle and Nuclear Physics **59**, 694 (2007).
- [55] L. N. Hand, D. G. Miller, and R. Wilson, Rev. Mod. Phys. **35**, 335 (1963).
- [56] S. Drell and J. Walecka, Annals of Physics **28**, 18 (1964).
- [57] L. I. Schiff, Phys. Rev. **83**, 252 (1951).
- [58] L. I. Schiff, Phys. Rev. **92**, 988 (1953).
- [59] Y.-Z. Chen, Y.-A. Luo, L. Li, H. Shen, and X.-Q. Li, Commun. Theor. Phys. **55**, 1059 (2011), arXiv:1101.3049 [hep-ph].
- [60] J. D. Lewin and P. F. Smith, Astropart. Phys. **6**, 87 (1996).
- [61] B. Döbrich, J. Jaeckel, F. Kahlhoefer, A. Ringwald, and K. Schmidt-Hoberg, JHEP **02**, 018 (2016), arXiv:1512.03069 [hep-ph].
- [62] K. Freese, J. Frieman, and A. Gould, Phys. Rev. D **37**, 3388 (1988).
- [63] R. Hofstadter, Rev. Mod. Phys. **28**, 214 (1956).
- [64] I. Sick, Nuclear Physics A **218**, 509 (1974).
- [65] B. Dreher, J. Friedrich, K. Merle, H. Rothhaas, and G. Lührs, Nucl. Phys. A **235**, 219 (1974).
- [66] G. Duda, A. Kemper, and P. Gondolo, JCAP **04**, 012 (2007), arXiv:hep-ph/0608035.
- [67] S. R. Klein and J. Nystrand, Phys. Rev. C **60**, 014903 (1999).
- [68] Y. Andreev *et al.* (NA64 Collaboration), Phys. Rev. Lett. **126**, 211802 (2021).
- [69] J. Mans (LDMX), EPJ Web Conf. **142**, 01020 (2017).
- [70] C.-Y. Chen, M. Pospelov, and Y.-M. Zhong, Phys. Rev. D **95**, 115005 (2017), arXiv:1701.07437 [hep-ph].
- [71] J. P. Lees *et al.* (BaBar), Phys. Rev. Lett. **119**, 131804 (2017), arXiv:1702.03327 [hep-ex].
- [72] T. Han, J. D. Lykken, and R.-J. Zhang, Phys. Rev. D **59**, 105006 (1999).